Mechanics Research Communications 42 (2012) 77–86

Contents lists available at SciVerse ScienceDirect

Mechanics Research Communications

journal homepage: www.elsevier.com/locate/mechrescom

Application of an anisotropic growth and remodelling formulation to computational structural design

Tobias Waffenschmidt [a,*], Andreas Menzel [a,b]

[a] Institute of Mechanics, Department of Mechanical Engineering, TU Dortmund, Leonhard-Euler-Str. 5, D-44227 Dortmund, Germany
[b] Division of Solid Mechanics, Lund University, P.O. Box 118, SE-22100 Lund, Sweden

ARTICLE INFO

Article history:
Received 21 October 2011
Received in revised form
19 December 2011
Available online 10 January 2012

Keywords:
Structural design
Anisotropic growth
Remodelling
Micro-sphere formulation
Finite element method

ABSTRACT

A classical structural optimisation problem consists of a problem-specific objective function which has to be minimised in consideration of particular constraints with respect to design and state variables. In this contribution we adopt a conceptually different approach for the design of a structure which is not based on a classical optimisation technique. Instead, we establish a constitutive micro-sphere-framework in combination with an energy-driven anisotropic microstructural growth formulation, which was originally proposed for the simulation of adaptation and remodelling phenomena in hard biological tissues such as bones.

The goal of this contribution is to investigate this anisotropic growth formulation with a special emphasis on its application to structural design problems. To this end, four illustrative three-dimensional benchmark-type boundary value problems are discussed and compared qualitatively with the results obtained by classical structural optimisation strategies. The simulation results capture the densification effects and clearly identify the main load bearing regions. It turns out, that even though making use of this conceptually different growth formulation as compared to the procedures used in a classical structural optimisation context, we identify qualitatively very similar structures or rather regions of densification. Moreover, in contrast to common structural optimisation strategies, which mostly aim to optimise merely the size, shape or topology, our formulation also contains the improvement of the material itself, which—apart from the structural improvement—results in the generation of problem-specific local material anisotropy and textured evolution.

1. Introduction

A typical task in solid-mechanics-related engineering consists in the development, improvement and optimisation of structures sustaining mechanical loads—in other words, to maximise the structural stiffness and/or to minimise the effective stress within the structure. In order to consistently treat and solve such structural optimisation problems, different rigorous mathematical formulations have been established. A classical structural optimisation problem consists of a problem-specific objective function, which has to be minimised in consideration of particular constraints with respect to design and state variables. The solution of such problems—if existent at all—is anything but trivial and commonly approximated by means of advanced numerical methods and algorithms for structural optimisation, cf. the extensive review of Bendsøe and Sigmund (2003). A structural optimisation problem is typically solved using a sequence of convex approximation in conjunction with Lagrangian duality. This approach results in a separable problem that enables an efficient numerical implementation, cf. Bendsøe and Sigmund (2003). For a discussion of such methods of convex approximations and their relations we refer to the textbook by Christensen and Klarbring (2009). Recently, structural optimisation problems have also been solved with a phase-field approach, see Wallin et al. (2011) and references cited therein.

In this contribution we adopt a conceptually different approach for the design of a structure, which is not based on a classical optimisation technique. We establish a constitutive micro-sphere-framework for energy-driven anisotropic microstructural growth and density evolution originally proposed for the simulation of isotropic adaptation phenomena in bones. Since the seminal work by Wolff (1892), it is well-known that bones are able to adapt their local density when exposed to mechanical loading. Such growth processes result in densification of the bone in regions of high loading levels and in degradation of the material in regions of low loading levels. This evolution process generates heterogeneous distributions of bone density accompanied by texture evolution and pronounced anisotropic material properties, as discussed by Taber (1995), Jacobs et al. (1997) and references cited therein.

* Corresponding author. Tel.: +49 231 755 3567; fax: +49 231 755 2688.
E-mail address: tobias.waffenschmidt@udo.edu (T. Waffenschmidt).

0093-6413/$ – see front matter © 2012 Elsevier Ltd. All rights reserved.
doi:10.1016/j.mechrescom.2011.12.004

The constitutive model used in this work is based on the so-called micro-sphere concept which allows to straightforwardly extend one-dimensional constitutive models to an anisotropic three-dimensional formulation, cf. the contribution by Bažant and Oh (1985), Kuhl et al. (2001) or Carol et al. (2004), Miehe et al. (2004) and Menzel and Waffenschmidt (2009) with regard to a large deformation framework. The constitutive approach, as proposed in this contribution, models bone growth within the framework of open system thermodynamics, as discussed by Kuhl and Steinmann (2003), using an enhanced balance of mass which models bone adaptation by its density evolution driven by the local strain energy level. We adopt the well-established model by Harrigan and Hamilton (1994) and extend this formulation to energy-driven evolution of directional densities which take, from the algorithmic point of view, the interpretation as internal variables, cf. the comparative overview by Kuhl et al. (2003) for a related discussion. These directional densities are referred to the integration direction of the micro-sphere and, as an advantage of the model at hand, enable to compute and visualise higher-order tensorial density moments which provide detailed insights into the simulated deformation-induced anisotropic local material properties, cf. Waffenschmidt et al. (2011). Common structural optimisation strategies mostly aim to optimise the size, shape or topology. Klarbring and Torstenfelt (2010, 2011) discuss the connection between an optimisation view and an evolution view. The formulation established as this work proceeds also contains improvement or rather adaptation of the local material properties themselves. This, apart from the structural design framework, results in an evolution of anisotropy and texture.

The manuscript is organised as follows: in Section 2, we briefly review relevant kinematic and balance relations for the micro-sphere-based density growth formulation. We investigate the finite element simulation of anisotropic growth with regard to its structure-improving properties by means of four illustrative numerical examples in Section 3 and conclude with a summary and final remarks in Section 4.

2. Model formulation

This section briefly reviews the model formulation used to simulate numerical examples later on in the context of structural design. The particular framework established in this work originates from the simulation of growth and remodelling phenomena in biological tissues. For a detailed outline including aspects on implementation of the model in a finite element framework the reader is referred to Waffenschmidt et al. (2011).

2.1. Basic kinematics and balance relations

As this work proceeds we set up an affine micro-sphere model. This approach allows use of well-established one-dimensional constitutive equations and to conveniently extend these to the three-dimensional case. As the model established is affine, the micro-sphere formulation allows similar conceptual interpretation as, for instance, Taylor-assumption-based models common for the simulation of polycrystalline materials.

To set the stage, we denote the non-linear motion of material placements $\boldsymbol{X} \in \mathcal{B}_0$ of particles of the body $\mathcal{B}$ of interest to their spatial position as $\boldsymbol{x} = \boldsymbol{\varphi}(\boldsymbol{X}, t) \in \mathcal{B}_t$, where t represents time. The motion's gradient in space is introduced as $\boldsymbol{F}$ and λ characterises the stretch in the direction of a referential unit-vector $\boldsymbol{r} \in \mathbb{U}^2$, i.e.

$$\boldsymbol{F} = \nabla_{\boldsymbol{X}} \boldsymbol{\varphi} \quad \text{and} \quad \lambda = \|\boldsymbol{t}\| = \|\boldsymbol{F} \cdot \boldsymbol{r}\| > 0. \tag{1}$$

The local form of the balance of mass—which intrinsically represents the growth process modelled as this work proceeds—as referred to the evolution of referential density ρ_0 reads

$$\dot{\rho}_0 = \nabla_{\boldsymbol{X}} \cdot \boldsymbol{R} + R_0, \tag{2}$$

wherein the notation $\dot{\bullet}$ denotes the material time derivative. Incorporation of Eq. (2) into the local referential balance of linear momentum relation, $[\rho_0 \dot{\boldsymbol{\varphi}}]^{\cdot} = \nabla_{\boldsymbol{X}} \cdot \boldsymbol{P} + \boldsymbol{b}_0$, results in

$$\rho_0 \ddot{\boldsymbol{\varphi}} = \nabla_{\boldsymbol{X}} \cdot [\boldsymbol{P} - \dot{\boldsymbol{\varphi}} \otimes \boldsymbol{R}] + [\boldsymbol{b}_0 - R_0 \dot{\boldsymbol{\varphi}} + \dot{\boldsymbol{F}} \cdot \boldsymbol{R}]. \tag{3}$$

In the following, however, we restrict the formulation to the quasi-static case and neglect the mass flux contribution as well as mechanical volume forces. It will turn out that this reduced framework with

$$\dot{\rho}_0 = R_0 \quad \text{and} \quad \boldsymbol{0} = \nabla_{\boldsymbol{X}} \cdot \boldsymbol{P}, \tag{4}$$

already nicely captures the structural design characteristics sought. So-called size effects, however, which can be modelled my means of the mass flux term $\boldsymbol{R}$, are excluded in the present formulation.

2.2. Constitutive equations

The subsequently elaborated constitutive equations are reduced to the one-dimensional case—with referential density ρ_0 and the stretch λ as a measure of deformation—so that the formulation can be extended to the three-dimension case by means of the micro-sphere framework later on. As an advantage, the numerical treatment is convenient to implement and, moreover, the three-dimensional micro-sphere-based growth model intrinsically includes deformation induced anisotropy and texture evolution. A hyperelastic form is assumed for the Piola stresses, in other words $\mathbf{P} = \partial_{\boldsymbol{F}} \psi_0$, whereas the referential density values are introduced as internal variables determined from the underlying evolution equations.

2.2.1. One-dimensional relations

We adopt a nowadays classical form for the density source term according to Harrigan and Hamilton (1993), to be specific

$$R_0 = k_\rho^* \left[\left[\frac{\rho_0}{\rho_0^*} \right]^{-m^*} \psi_0 - \psi_0^* \right], \tag{5}$$

with k_ρ^*, ρ_0^*, m^* and ψ_0^* being material parameters and so-called dead zones being neglected. Eq. (5) enables saturation-type local density evolution, which does not allow to control the total mass directly. In other words, the driving energy term $[\rho_0/\rho_0^*]^{-m^*} \psi_0$ must decrease with increasing normalised referential density ρ_0/ρ_0^* and vice versa. This can be guaranteed by introducing the density-weighted strain energy

$$\psi_0 = \left[\frac{\rho_0}{\rho_0^*} \right]^{n^*} \psi_0^{\mathrm{e}}(\lambda), \tag{6}$$

wherein $\psi_0^{\mathrm{e}}(\lambda)$ monotonically increases with λ and the material parameter is constrained by $n^* < m^*$. The specific form chosen for the elastic strain energy contribution is of neo-Hookean type, which in its one-dimensional representation reads

$$\psi_0^{\mathrm{e}}(\lambda) = \frac{\lambda^*}{2} \ln^2(\lambda) + \frac{\mu^*}{2} [\lambda^2 - 1 - 2 \ln(\lambda)], \tag{7}$$

including two additional parameters, λ^* and μ^* which, for the model at hand, do not address different modes of deformation.

In classical structural optimisation formulations, it is common to prescribe an upper and lower bound for the density. Even if not applied to the simulations following in Section 3, lower and upper bounds for the density ρ_0 can be straightforwardly incorporated

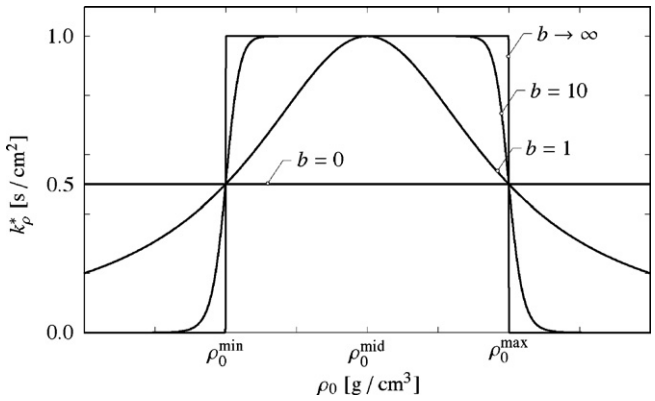

Fig. 1. Generalised bell function as introduced in Eq. (8), plotted for different values of b. For $b=0$ the original approach without any bounds is restored (here referred to a constant value of $k_\rho^* = 0.5$) whereas for $b \to \infty$ a sharp lower and upper bound can be included by means of the parameters $\rho_0^{\min}$ and $\rho_0^{\max}$ respectively.

in the present approach, for example by means of replacing the constant growth velocity k_ρ^* by a function in ρ_0. As one possibility among others, a generalised bell function defined as

$$k_\rho^*(\rho_0) = \frac{1}{1 + \left|[\rho_0 - \rho_0^{\mathrm{mid}}]/[\rho_0^{\max} - \rho_0^{\mathrm{mid}}]\right|^{2b}} \quad \text{with } \rho_0^{\mathrm{mid}} = \frac{\rho_0^{\max} + \rho_0^{\min}}{2} \tag{8}$$

can be introduced, thereby restricting the density to vary between the bounds $\rho_0^{\min}$ and $\rho_0^{\max}$. The bell function (8) is visualised in Fig. 1 for different values of b, where $b \geq 0$ and $\rho_0^{\min} < \rho_0^* < \rho_0^{\max}$.

2.2.2. Three-dimensional micro-sphere framework

The three-dimensional micro-sphere formulation is based on integration of one-dimensional constitutive relations on the unit-sphere $\mathbb{U}^2$. Including a normalisation, the notation for the general integration operation is introduced as

$$\langle \bullet \rangle = \frac{1}{4\pi} \int_{\mathbb{U}^2} \bullet \, \mathrm{d}A. \tag{9}$$

Based on this, the hyper-elastic form for the Piola stresses is now determined from the density-weighted strain energy $\psi_0 = \langle \psi_0(\lambda) \rangle$ and takes the representation

$$\boldsymbol{P} = \frac{\partial \psi_0}{\partial \boldsymbol{F}} = \left\langle \frac{\partial \psi_0}{\partial \lambda} \frac{\partial \lambda}{\partial \boldsymbol{F}} \right\rangle = \left\langle \left[\frac{\rho_0}{\rho_0^*}\right]^{n^*} \frac{\partial \psi_0^{\mathrm{e}}}{\partial \lambda} \frac{1}{\lambda} \boldsymbol{t} \otimes \boldsymbol{r} \right\rangle, \tag{10}$$

cf. Eqs. (1) and (6). It is important to note that both, the stretch λ as well as the referential density ρ_0 are referred to the direction of the referential unit-vector $\boldsymbol{r} \in \mathbb{U}^2$. Moreover, the unit-sphere itself should not be confused with a representative volume element since the unit-sphere does not take the interpretation of a physical space.

The integration operation introduced in Eq. (9) is generally too complicated to be evaluated analytically so that numerical integration schemes are applied.

2.2.3. Higher-order referential density moments

The directional referential density ρ_0 takes different values for different levels of deformation λ. As these stretches λ depend on the motion gradient $\boldsymbol{F}$ and the respective direction $\boldsymbol{r}$, the direction dependent density values render the constitutive relation for the Piola stresses $\boldsymbol{P}$ to be anisotropic. This texture can be represented by means of different anisotropy quantities and visualisation techniques, such as directional Young's moduli plots. In this work we make use of higher-order referential density moments, which are defined by means of Eq. (9) as

$$A = \langle \rho_0 \rangle, \tag{11}$$

$$\boldsymbol{A} = 3\langle \rho_0 \boldsymbol{r} \otimes \boldsymbol{r} \rangle, \tag{12}$$

$$\mathbf{A} = 5\langle \rho_0 \boldsymbol{r} \otimes \boldsymbol{r} \otimes \boldsymbol{r} \otimes \boldsymbol{r} \rangle, \tag{13}$$

so that $\rho_0 = 1$ renders A, $\boldsymbol{A}$ and $\mathbf{A}$ as (symmetric) identity tensors of zeroth, second and fourth order.

3. Finite element simulations

This section covers illustrative structural-design-related examples based on the anisotropic micro-sphere growth formulation as summarised in Section 2. Motivated by Borrvall and Petersson (2001), we investigate four three-dimensional benchmark-type problems.

In view of the material parameters used for the following examples, we adopt the values summarised in Table 1 and choose a constant time step size of $\Delta t = 0.5$ s for all simulations. Furthermore, the loading magnitude $f = \delta\tau$ is defined in terms of the respective traction magnitude τ multiplied by the stepwise load scaling parameter δ, see Fig. 2. The local densities ρ_0^i, as referred to the underlying discrete integration directions $\boldsymbol{r}_i \in \mathbb{U}^2$—with $i = 1, \ldots, 21$ as this work proceeds, cf. Bažant and Oh (1986)—are stored as internal variables at the finite element integration point level, with $\rho_0^i\big|_{t_0} = \rho_0^*$. In consequence, the model becomes path-dependent. Local anisotropic material properties are visualised via Eqs. (11)–(13) by means of orientation-distribution-function-type (odf) representations, as shown in Section 3.5, see also Waffenschmidt et al. (2011).

3.1. Cantilever

As a first example, we consider a cantilever, see Fig. 3(a), with $L = 100$ mm. Its back side is clamped while a square region of the

Table 1
Set of material parameters used for the calculations.

Parameter	Value	Unit
λ^*	2186.0	[N/mm^2]
μ^*	1458.0	[N/mm^2]
ρ_0^*	1.0	[g/cm^3]
ψ_0^*	0.01	[N/mm^2]
k_ρ^*	0.4	[s/cm^2]
n^*	2.0	[–]
m^*	3.0	[–]

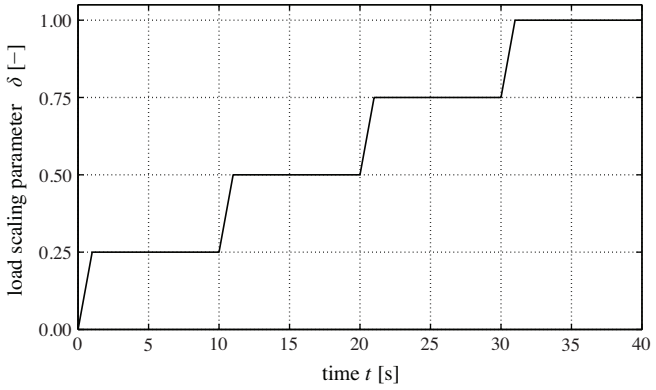

Fig. 2. Stepwise constant load scaling parameter δ used for the simulations. The magnitude of the respective loading is $f = \delta\tau$, where τ is specified for the respective examples.

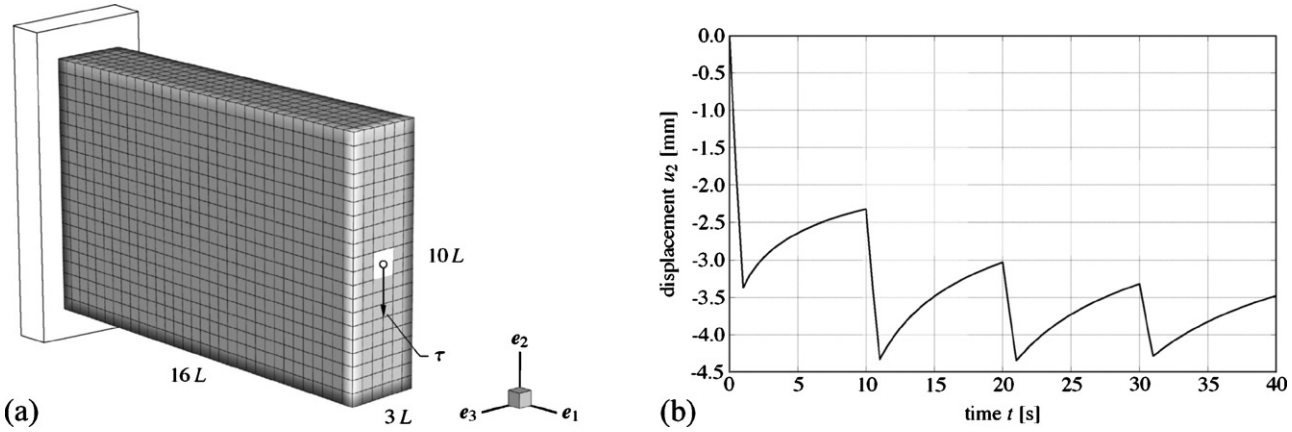

Fig. 3. (a) Geometry, finite element mesh and boundary conditions of the cantilever. The back side of the beam is clamped while the white region at the front of the beam is exposed to shear traction τ. (b) Evolution of displacement $u_2 = \boldsymbol{u} \cdot \boldsymbol{e}_2$ recorded at middle node (○) within white region at front side.

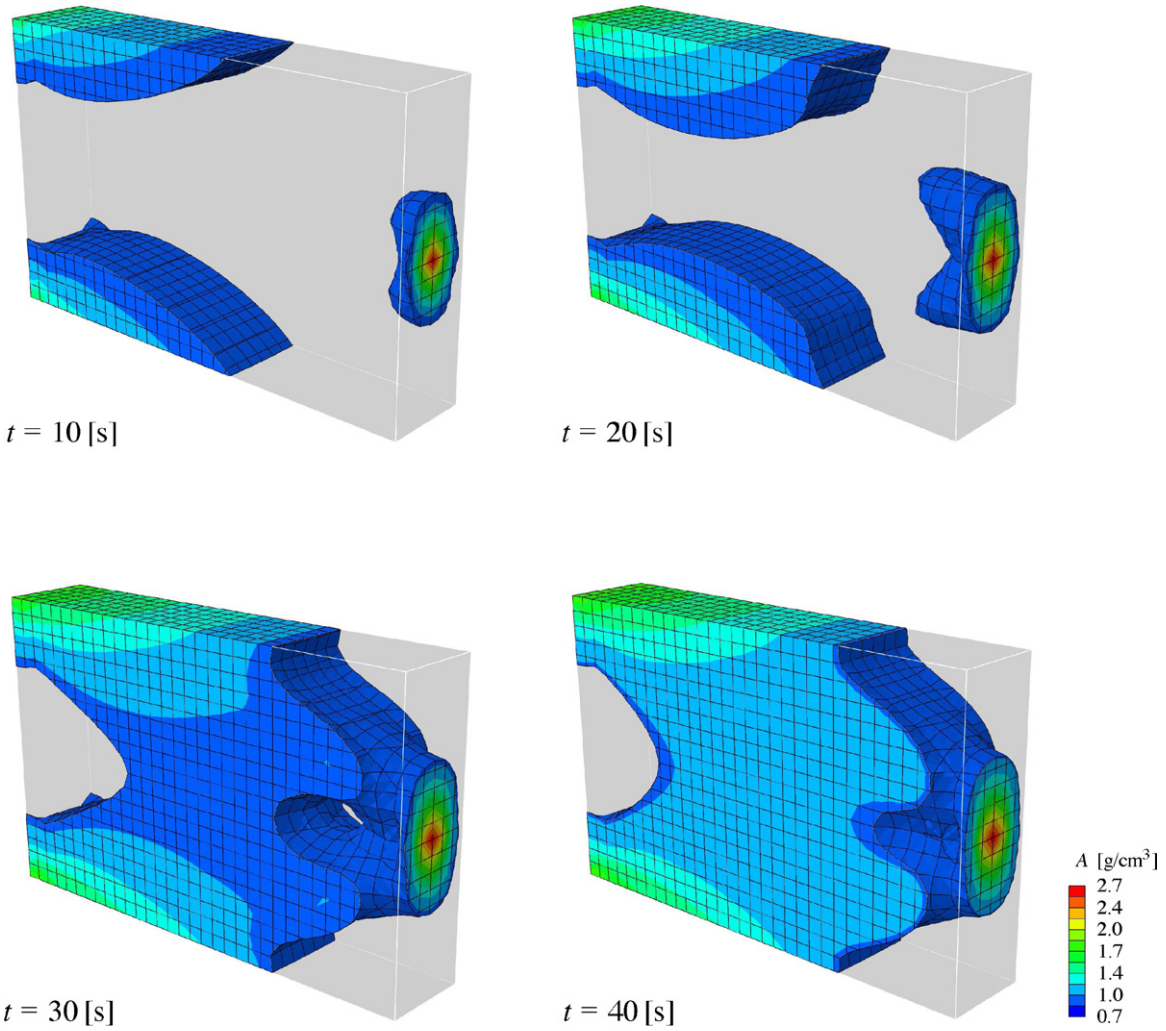

Fig. 4. Finite element simulation of the cantilever exposed to shear traction, cf. Borrvall and Petersson (2001). Evolution of the zeroth-order density moment A at four different points in time where regions with values of $A < \rho_0^*$ are blanked.

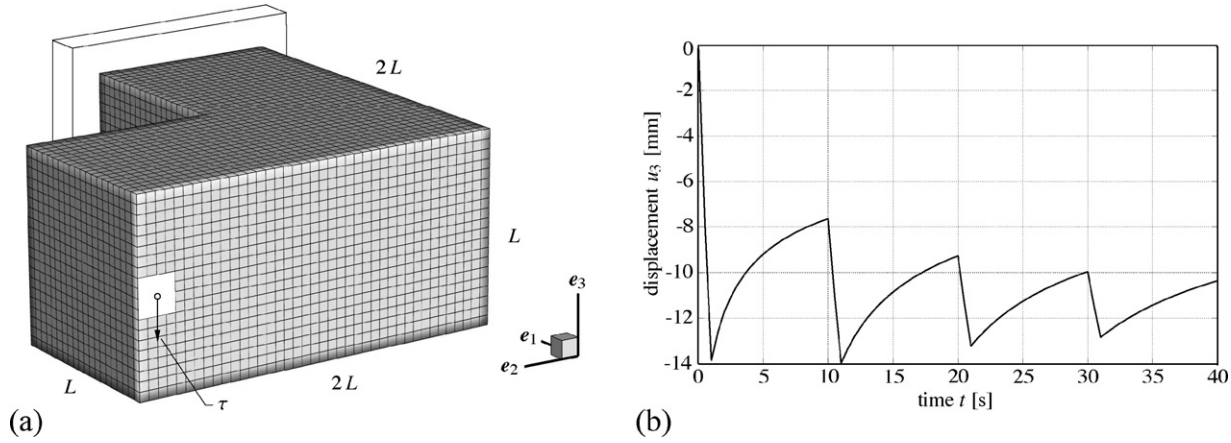

Fig. 5. (a) Geometry, finite element mesh and boundary conditions of the crank. The back side of the crank is clamped while the white region at the front of the crank is exposed to shear traction τ. (b) Evolution of displacement $u_3 = \boldsymbol{u} \cdot \boldsymbol{e}_3$ recorded at middle node (○) within the white region at the front side.

front is loaded by a shear traction in vertical direction, i.e. $\boldsymbol{\tau} = -\delta\tau\boldsymbol{e}_2$ with $\tau = 1.6\,\mathrm{N/mm^2}$. The cantilever is discretised with $32 \times 20 \times 6$ linear displacement-based hexahedral elements with 4851 nodes.

The deformation in terms of the vertical displacement $u_2 = \boldsymbol{u} \cdot \boldsymbol{e}_2$ recorded at the middle node (○) of the white loading region over time is plotted in Fig. 3(b). Due to the stepwise application of constant shear traction forces, we observe a distinct creep-type adaptation behaviour. The magnitude of the displacement clearly tends to decrease with time for a constant loading level $\boldsymbol{\tau}$, which results from the adaptation process accompanied by a change in local density A and corresponds to an increase in stiffness respectively a decrease in compliance. However, we observe that the displacement highlighted tends to saturate towards a characteristic equilibrium state—a state where the deformation and the density remains constant for a given load, but does not fully reach this state for any of the loading levels. To capture these saturation plateaus, one could either increase the time period of the constant loading levels or increase the adaptation velocity k_ρ^*, see Waffenschmidt et al. (2011) for a detailed sensitivity-type analysis of the material parameters.

To analyse the growth or rather structural design process in the cantilever under the prescribed loading conditions, we display the evolution of the zeroth-order density moment A at four different points in time, $t = \{10, 20, 30, 40\}$ s, see Fig. 4. Here and in the following, degrading regions corresponding to values of $A < \rho_0^*$ are blanked which means that only isosurfaces corresponding to a densification of the material, i.e. $A \geq \rho_0^*$, are visible. However, the blanked degenerated regions still exist and also contribute to the overall load-bearing capacity.

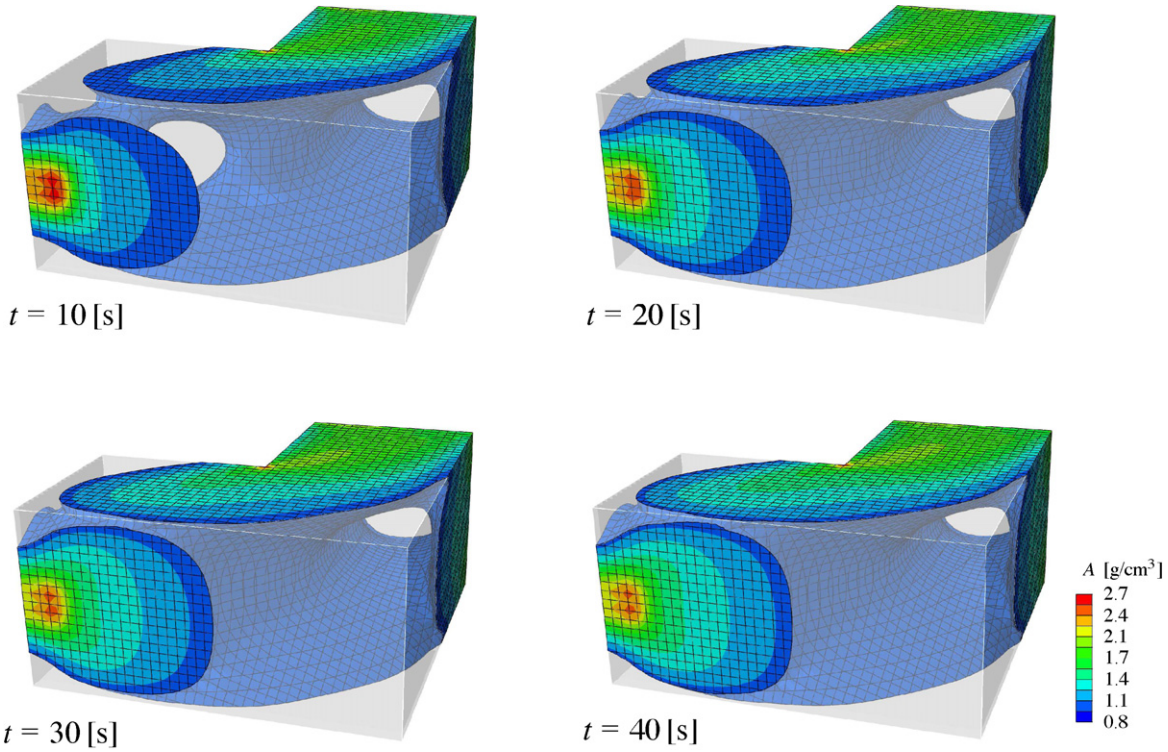

Fig. 6. Finite element simulation of the crank exposed to shear traction, cf. Borrvall and Petersson (2001). Evolution of the zeroth-order density moment A at four different points in time where regions with values of $A < \rho_0^*$ are blanked.

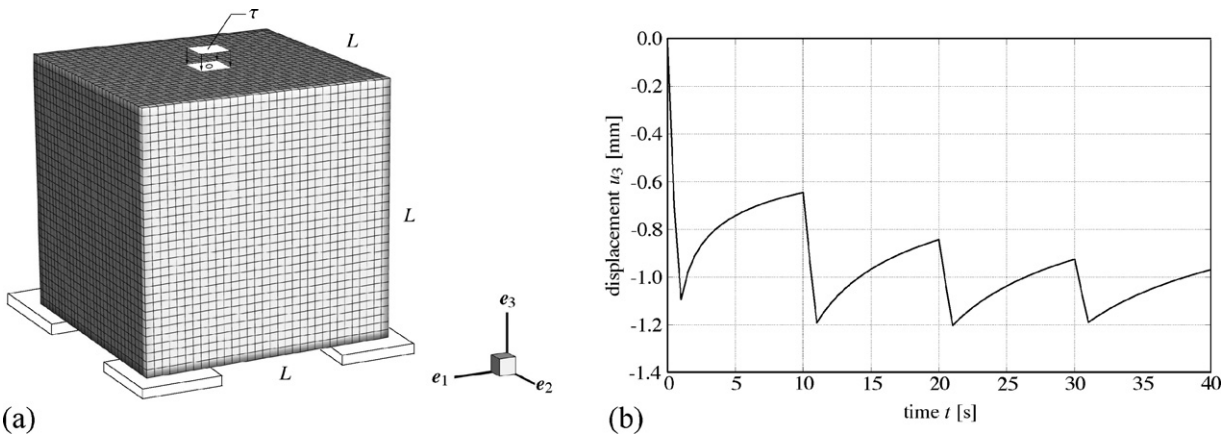

Fig. 7. (a) Geometry, finite element mesh and boundary conditions of the stool. Four square regions at the bottom edges are clamped while a square region on top of the cube is loaded by means of a traction in vertical direction. (b) Evolution of displacement $u_3 = \boldsymbol{u} \cdot \boldsymbol{e}_3$ recorded at middle node (◦) within white region at the top side.

In Fig. 4, we observe a remarkable densification of the cantilever after 10 s particularly in those regions that are predominantly affected by the loading and in consequence associated with high levels of strain energy. For the problem at hand, these regions are the load-bearing upper and lower flanges of the cantilever as well as the region where the traction is applied. At 40 s, the expected distribution of the material, such that the cantilever provides improved structural support for the applied shear traction, is observed. Compared to the distribution obtained by Borrvall and Petersson (2001), we find qualitatively similar results for the cantilever example, even if the reported "I-beam design with varying dimensions of waist and flanges" cannot be reproduced exactly and the blanked degenerated regions still contribute to the overall load-carrying capacity. Moreover, the discretisation in

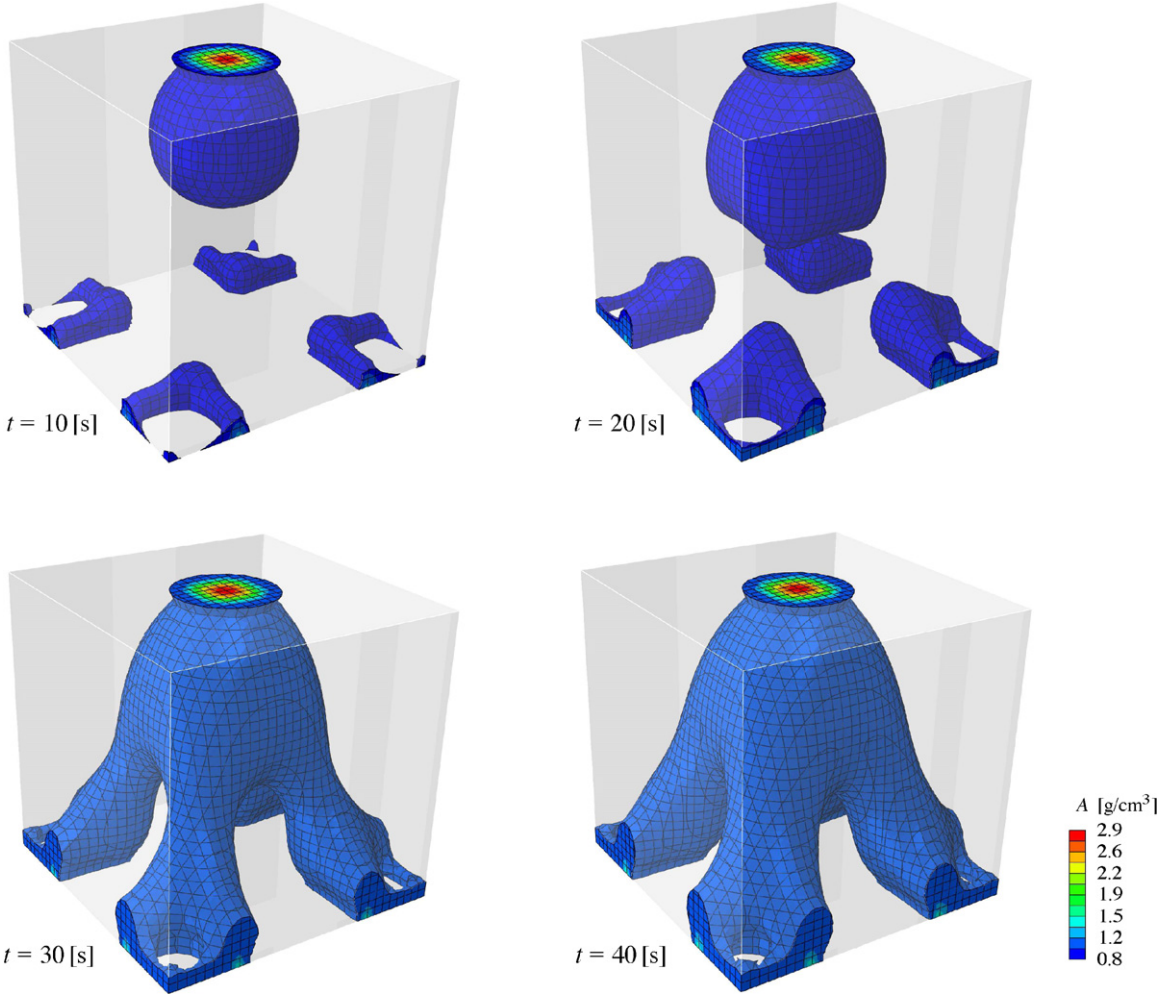

Fig. 8. Finite element simulation of the stool exposed to traction, cf. Borrvall and Petersson (2001). Evolution of the zeroth-order density moment A at four different points in time where regions with values of $A < \rho_0^*$ are blanked.

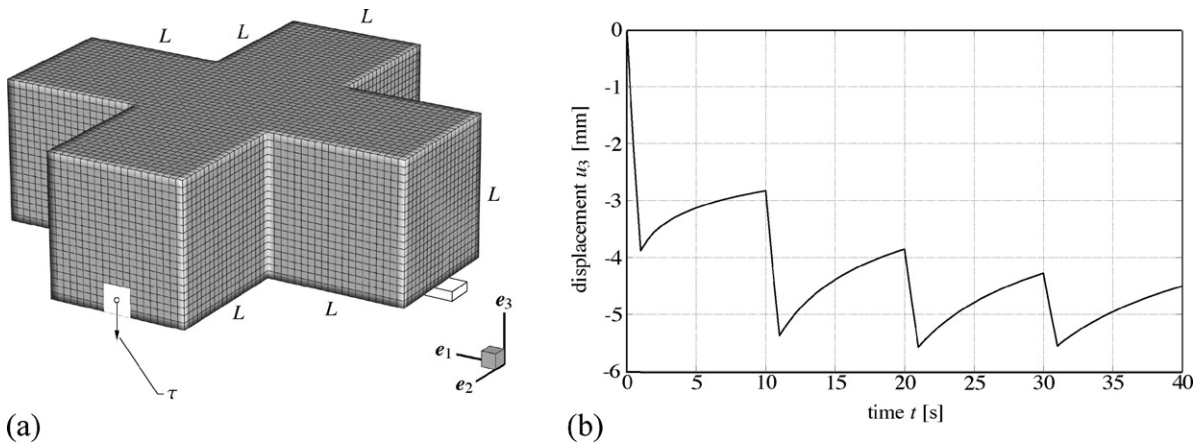

Fig. 9. (a) Geometry, finite element mesh and boundary conditions of the coathanger. Clamped square regions of the lateral parts of the cross while shear tractions are applied at small square regions at the front and the back of the domain. (b) Evolution of displacement $u_3 = \boldsymbol{u} \cdot \boldsymbol{e}_3$ recorded at middle node (○) within white region at the front side.

the present study is much coarser—we use only 6 elements over the width of the beam whereas Borrvall and Petersson (2001) use 24 elements.

3.2. Crank

As the second example, we consider an L-shaped crank structure with $L = 100$ mm. The back side is clamped ($u_1 = u_2 = u_3 = 0$) while a shear traction of $\boldsymbol{\tau} = -\delta\tau\boldsymbol{e}_3$ with $\tau = 1.5\,\mathrm{N/mm^2}$ is applied at a small square region at the front of the crank, cf. Fig. 5(a). The geometry is discretised by 24,000 displacement-based quadrilateral finite elements resulting in 26,901 nodes.

The deformation in terms of the vertical displacement $u_3 = \boldsymbol{u} \cdot \boldsymbol{e}_3$ recorded at the middle node (○) within the white loading region over time is plotted in Fig. 5(b). Compared to Fig. 3(b), a qualitatively similar mechanical response is observed. Fig. 6 illustrates the evolution of the zeroth-order density moment A at four different points in time where regions with values of $A < \rho_0^*$ are blanked. Even if we use only 24,000 finite elements, the resulting structure is very similar to the results reported by Borrvall and Petersson (2001) who applied 256,000 elements. The present loading case leads to a combination of bending and torsion: we observe a slanting I-beam character at the outer part of the structure as a result of the bending, while close to the clamped wall the improved shape consists of a tubular section which stems from the torsional loading.

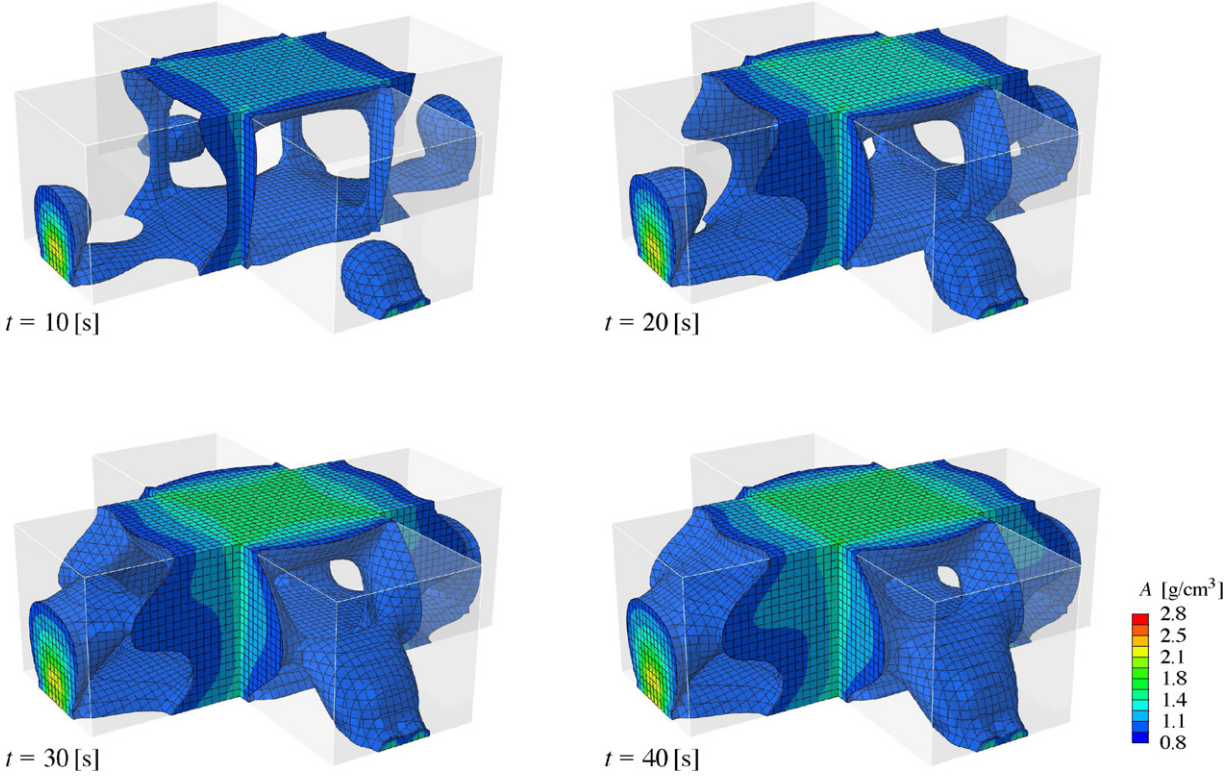

Fig. 10. Finite element simulation of the coathanger exposed to shear traction, cf. Borrvall and Petersson (2001). Evolution of the zeroth-order density moment A at four different points in time where regions with values of $A < \rho_0^*$ are blanked.

3.3. Stool

As a third example, we consider a cube, see Fig. 7(a), with $L = 100$ mm. We apply the loading at the top of the cube by means of a traction in vertical direction, i.e. $\tau = -\delta\tau \boldsymbol{e}_3$ with $\tau = 5.0\,\mathrm{N/mm^2}$ and clamp the cube at four square edge regions at the edges. In the work by Borrvall and Petersson (2001), however, these regions are supported only in $\boldsymbol{e}_3$-direction with the displacements in $\boldsymbol{e}_1$- and $\boldsymbol{e}_2$-direction being unconstrained. The cube is discretised into $32 \times 32 \times 32$ linear displacement-based hexahedral elements with 35,937 nodes.

The evolution of the vertical displacement $u_3 = \boldsymbol{u} \cdot \boldsymbol{e}_3$ recorded at the middle node (○) within white region is plotted in Fig. 7(b).

Fig. 8 shows the evolution of A at four different points in time where regions with values of $A < \rho_0^*$ are blanked. Similar to Borrvall and Petersson (2001), we observe that the resulting structure consists of four legs which somewhat resemble the design of a stool. For the simulations performed in this work, however, the lower parts of the legs of the stool are separated from each other, whereas in Borrvall and Petersson (2001) the legs are kept together by a plate on the floor. This effect stems from the specific boundary conditions chosen.

3.4. Coathanger

The last example consists of a cross-shaped domain, see Fig. 9(a) where $L = 100$ mm, which is discretised into 40,000 linear displacement-based hexahedral elements resulting in 44,541 nodes. As boundary conditions, we apply shear tractions of $\boldsymbol{\tau} = -\delta\tau \boldsymbol{e}_3$ with $\tau = 1.0\,\mathrm{N/mm^2}$ at small square regions at the front and the back side of the specimen while we clamp the displacements at square regions of the lateral parts of the cross.

The vertical displacement $u_3 = \boldsymbol{u} \cdot \boldsymbol{e}_3$ recorded at the middle node (○) within the white region over time is displayed in Fig. 9(b).

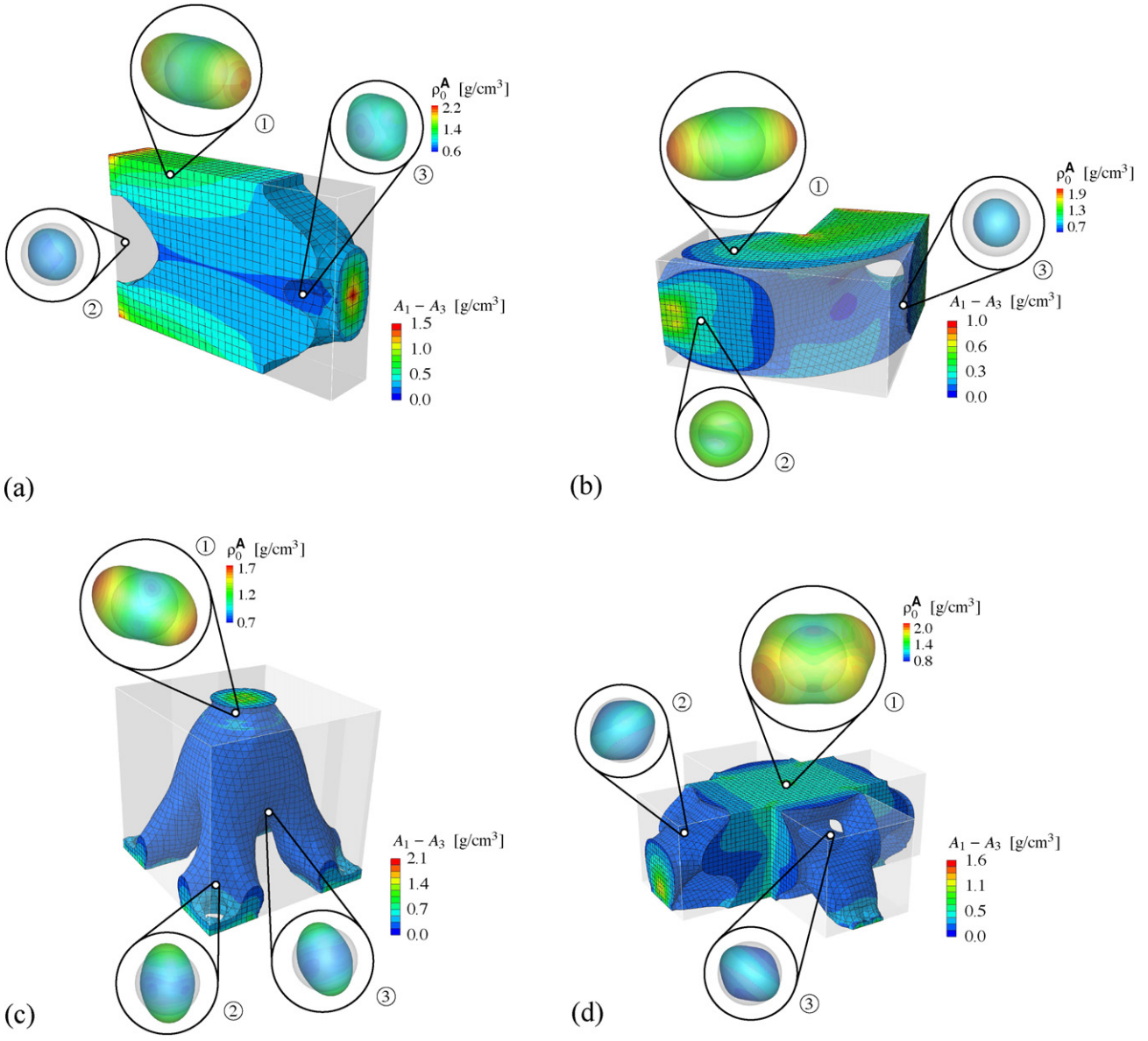

Fig. 11. Anisotropy evolution for the four examples (a)–(d) at $t = 40$ s displayed at representative integration points and visualised by means of odf-type distributions based on fourth-order density moments **A**, whereby the isotropic initial state is plotted additionally as a reference state (grey-shaded sphere). A change in size of the odf is attributed to densification/degradation; a change in shape of the odf is attributed to the evolution of anisotropic material properties. The colour code respectively contour plot, indicates the evolution of the anisotropy by means of visualising the difference between the maximum and minimum principal value of $\boldsymbol{A}$, i.e. $A_1 - A_3$. (For interpretation of the references to colour in this figure legend, the reader is referred to the web version of the article.)

Fig. 10 shows the evolution of A at four different points in time where regions with values of $A < \rho_0^*$ are blanked. Similar to Borrvall and Petersson (2001), we observe that the resulting structure resembles the design of a coathanger. It is interesting to see that the evolving improved density distribution consists of a plane surface in the upper middle part of the cross supporting tensile stresses and a plate at the bottom reaching from the front to the back loading regions and thereby supporting compressive stresses.

3.5. Evolution of anisotropy

Since the growth process modelled in this contribution is anisotropic, we additionally investigate the evolution of anisotropy by means of representative anisotropy measures. As a scalar-valued quantity we use the difference in maximum and minimum principal values of the second-order density moment $\boldsymbol{A} = A_i \boldsymbol{n}_i \otimes \boldsymbol{n}_i$, i.e. $A_1 - A_3$, cf. Eq. (12). This anisotropy measure is depicted as a contour plot for all four examples in Fig. 11 at $t = 40$ s, where an isotropic state (blue) corresponds to $A_1 - A_3 = 0$. It is clearly seen that the degree of anisotropy changes most significantly in those regions which are predominantly loaded and thus undergo high strain energy levels.

To investigate the evolution of anisotropy in more detail, we now focus on three exemplary integration points to visualise local anisotropic material properties by means of the fourth-order moment $\mathbf{A}$ or rather its corresponding orientation-distribution-type-function (odf) $\rho_0^{\mathbf{A}} = [\boldsymbol{r} \otimes \boldsymbol{r}] : \mathbf{A} : [\boldsymbol{r} \otimes \boldsymbol{r}]$.

Fig. 11(a) shows the local state of anisotropy at three different integration points for the cantilever. As intuitively expected, we see that odf ① located at the top load-bearing "flange" of the cantilever shows the most significant change in size and shape, which reflects a pronounced growth behaviour accompanied by a considerable change of anisotropic material properties. Odf ③, evaluated near the loading region, also shows moderate anisotropic behaviour or rather texture evolution, since its shape deviates from its initial spherical distribution which, here and in the following, is marked by the superimposed grey-shaded sphere. Odf ②, however, shrinks almost isotropically, i.e. maintaining its spherical shape, which clearly indicates the degradation process of the material located in this point.

By analogy to the considerations above, Fig. 11(b) illustrates the local state of anisotropy at three different integration points for the crank example. We observe that especially odf ① shows a very pronounced and elongated shape in combination with a drastic change in size. This distribution corresponds to an almost transversely isotropic state, similar to odf ① of the cantilever. Odf ②, located near the loading region, shows moderate anisotropic properties, whereas odf ③ shrinks isotropically which clearly indicates the degradation process of the material located in this point.

Similarly, Fig. 11(c) and (d) illustrates the local anisotropy for the stool and the coathanger. In both cases, especially odfs ① show a very pronounced anisotropic shape in combination with a considerable change in size. Odfs ② and ③ show only moderate anisotropic behaviour.

4. Summary

This contribution investigates the application of a constitutive model which was originally proposed for the simulation of anisotropic growth and remodelling phenomena in bones to structural design. To this end, four three-dimensional benchmark-type problems, taken from topology-optimisation-related literature as e.g. Borrvall and Petersson (2001), are discussed and compared qualitatively with the results obtained by the aforementioned authors.

The constitutive model proposed in this work is based on the micro-sphere framework which allows to straightforwardly extend one-dimensional constitutive models to an anisotropic three-dimensional formulation. The well-established one-dimensional model includes energy-driven evolution of directional densities. These directional densities are referred to the integration direction of the micro-sphere and, as an advantage of the model at hand, enable to compute higher-order tensorial density moments. By analogy to so-called Young's moduli plots common in the context of modelling and simulation of texture phenomena, the visualisation of such higher-order density moments provides detailed insights into the simulated deformation-induced anisotropic local material properties.

The simulation results capture the densification effects and clearly identify the main load bearing regions. In this regard, degrading regions are blanked for illustration and comparison purposes which means that only isosurfaces corresponding to a densification of the material are visible. However, the blanked degenerated regions still exist and contribute to the overall load-bearing capacity. In this regard, one may also think of a complete removal of the degrading regions followed by a subsequent simulation with a new discretisation.

It turns out that even if we take a conceptually different approach compared to the procedures used in the more classical topology-optimisation context by Borrvall and Petersson (2001), we nevertheless find—at least qualitatively—very similar designs by blanking regions of degradation. Apart from the totally different material model allowing for large deformations, present discrepancies can partly be attributed to the coarser discretisation and slightly different application of boundary conditions. Moreover, in contrast to common structural optimisation strategies, which mostly aim to optimise merely the size, shape or topology, the formulation proposed in this work also contains the improvement or rather adaptation of the material properties itself. This consequently results in an evolution of anisotropy and texture, which—by means of the material model proposed—can be conveniently visualised in terms of orientation-distribution-function-type representations of higher-order density moments. This additional information can, from a material design point of view, be very valuable—in particular in combination with the structural design formulation established.

References

Bažant, Z., Oh, B., 1985. Microplane model for progressive fracture of concrete and rock. Journal of Engineering Mechanics 111, 559–582.

Bažant, Z., Oh, B., 1986. Efficient numerical integration on the surface of a sphere. Zeitschrift für angewandte Mathematik und Mechanik 66, 37–49.

Bendsøe, M.P., Sigmund, O., 2003. Topology Optimization – Theory, Methods and Applications. Springer.

Borrvall, T., Petersson, J., 2001. Large-scale topology optimization in 3D using parallel computing. Computer Methods in Applied Mechanics and Engineering 190, 6201–6229.

Carol, I., Jirásek, M., Bažant, Z., 2004. A framework for microplane models at large strain, with application to hyperelasticity. International Journal of Solids and Structures 41, 511–557.

Christensen, P.W., Klarbring, A., 2009. An Introduction to Structural Optimization. Springer.

Harrigan, T., Hamilton, J., 1993. F inite element simulation of adaptive bone remodelling: a stability criterion and a time stepping method. International Journal for Numerical Methods in Engineering 36, 837–854.

Harrigan, T., Hamilton, J., 1994. Necessary and sufficient conditions for global stability and uniqueness in finite element simulations of adaptive bone remodelling. International Journal of Solids and Structures 31, 97–107.

Jacobs, C.R., Simo, J.C., Beaupré, G.S., Carter, D.R., 1997. Adaptive bone remodeling incorporating simultaneous density and anisotropy considerations. Journal of Biomechanics 30, 603–613.

Klarbring, A., Torstenfelt, B., 2010. Dynamical systems and topology optimization. Structural and Multidisciplinary Optimization 42, 179–192.

Klarbring, A., Torstenfelt, B., 2011. Dynamical systems, SIMP, bone remodeling and time dependent loads. Structural and Multidisciplinary Optimization.

Kuhl, E., Menzel, A., Steinmann, P., 2003. Computational modeling of growth – a critical review, a classification of concepts and two new consistent approaches. Computational Mechanics 32, 71–88.

Kuhl, E., Steinmann, P., 2003. Theory and numerics of geometrically non-linear open system mechanics. International Journal for Numerical Methods in Engineering 58, 1593–1615.

Kuhl, E., Steinmann, P., Carol, I., 2001. A thermodynamically consistent approach to microplane theory. Part II. Dissipation and inelastic constitutive modeling. International Journal of Solids and Structures 38, 2933–2952.

Menzel, A., Waffenschmidt, T., 2009. A micro-sphere-based remodelling formulation for anisotropic biological tissues. Philosophical Transactions of the Royal Society A 367, 3499–3523.

Miehe, C., Göktepe, S., Lulei, F., 2004. A micro–macro approach to rubber-like materials. Part I. The non-affine micro-sphere model of rubber elasticity. Journal of the Mechanics and Physics of Solids 52, 2617–2660.

Taber, L., 1995. Biomechanics of growth, remodelling, and morphogenesis. American Society of Mechanical Engineers – Applied Mechanics Reviews 48, 487–545.

Waffenschmidt, T., Menzel, A., Kuhl, E., 2011. Anisotropic density growth of bone – a computational micro-sphere approach, submitted for publication.

Wallin, M., Ristinmaa, M., Askfelt, H., 2011. Optimal topologies derived from a phase-field method. Structural and Multidisciplinary Optimization, 1–13, doi:10.1007/s00158-011-0688-x.

Wolff, J., 1892. Das Gesetz der Transformation der Knochen. Hirschwald, Berlin.